ELSEVIER

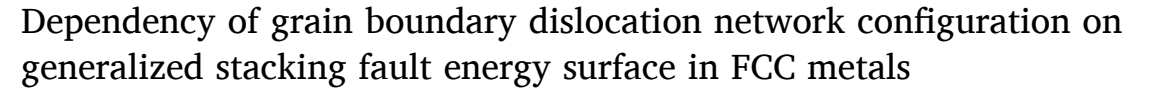
Contents lists available at ScienceDirect

# Computational Materials Science

journal homepage: www.elsevier.com/locate/commatsci



# Full Length Article



Yongxiang Li<sup>a</sup>, Di Qiu<sup>a,c,\*</sup>, Yunzhi Wang<sup>b</sup>

- a Materials Genome Institute, Shanghai University, 333 Nan Chen Road, Shanghai 200444, China
- b Department of Materials Science and Engineering, The Ohio State University, 2041 College Road, Columbus, OH 43210, USA
- <sup>c</sup> Zhejiang Laboratory, Hangzhou, Zhejiang 311100, China

## ARTICLE INFO

Keywords: Stacking faults Dislocation dissociation Grain boundary structure Phase-field modeling

## ABSTRACT

We use a microscopic phase-field (MPF) model, incorporating the generalized stacking fault energy (GSFE) surfaces (i.e., the  $\gamma$ -surface) as inputs, to investigate systematically the evolution of dislocation network configurations at low-angle pure twist grain boundaries (GBs) in six face-centered cubic (FCC) metals (Ag, Cu, Rh, Ir, Pd and Pt) that have different GSFE surfaces. The equilibrium configurations of GB dislocation networks are obtained via the interplay between the crystalline energy and the elastic strain energy during the energy minimization process. It was found that for {111} twist GBs, though the geometrically necessary dislocations (GNDs) of the screw type are observed, they can be either full or partial ones depending on the GSFE surfaces of the above metal systems. The areas of the staking faults regions formed between partial dislocations are quantitatively characterized as a function of the magnitude of the stacking fault energy, the elastic modulus and the GB misorientation angle. A fast-acting model for predicting the geometric characteristics of the GB dislocation networks is developed based directly on the material properties and GB misorientation, which is validated by its applications to another two metal systems (Au and Ni) with the same GB.

#### 1. Introduction

Both physical and mechanical properties of polycrystalline materials are significantly impacted by the structures of grain boundaries (GBs) [1], and GB engineering has been one of the key subjects in physical metallurgy for many decades. GB energy is known to be anisotropic, depending on both the crystal structure and the five degrees of freedom (DOF) of a GB and is therefore difficult to quantify [2,3]. Moreover, the intricate atomic interactions at GBs alter impurity contents at GBs (deviate from those in the bulk) and, consequently, influence their structures (e.g., phase transitions or complexion transitions) and energy [4].

Computationally, molecular dynamics (MD) with empirical potentials and density functional theory (DFT) calculations are commonly used to study the structures and properties of GBs. For example, with the technique of embedded atom method (EAM), researchers have gained a better understanding of the atomic structures and energies of GBs in pure metals [5–7]. Moreover, Holm et al. [8] found that the energies of GBs in different materials are strongly correlated with the stacking fault energy (SFE) after calculating more than 300 GBs in Al, including

general and special  $\Sigma$  GBs using atomistic simulations that were developed for GBs with both CSL misorientations and rational boundary plane normal under certain simulation cell constrains [9]. However, MD simulations are limited by the availability of high-quality interatomic potentials that can reproduce the ab initio GSFE surface, and it can be challenging for these potentials to account for more than two element types [10,11] due to the size scale and complexities caused by the mutual interactions among different elements. The DFT calculations, though offering high accuracy, can only be applied to a small set of specific GBs due to the limited computational-cell size that can be considered. On the other hand, geometric approaches such as O-lattice theory [12] and Frank-Bilby model [13,14] have been developed over the past decades to provide direct predictions of dislocation networks formed by geometrically necessary dislocations (GNDs) based on the macroscopic DOFs of GBs, and the 3D polyhedral unit model first proposed by Ashby et al. [15] has recently been improved through an algorithm based on Voronoi network that was used to automatically capture the polyhedral structure of symmetric/asymmetric tilt and twist GBs in FCC metals [16]. Nevertheless, these predictions are essentially based solely on geometric analysis without considering the underlying

<sup>\*</sup> Corresponding author at: Materials Genome Institute, Shanghai University, 333 Nan Chen Road, Shanghai 200444, China. *E-mail address*: diqiu0319@shu.edu.cn (D. Qiu).





free energy or force-field and, thus, not suitable for studying the formation mechanism and dynamic evolution of GB GND networks. In addition, GB models are expected to be coupled with mesoscale property models so that multi-scale modeling can be carried out to predict GB structures and their impacts on material properties.

In order to overcome these difficulties, Shen et al. [10,11] incorporated the generalized stacking fault energy (GSFE) surfaces from DFT calculations into a microscopic phase field model (MPF), which is essentially a generalization of the Peierls model of dislocations [17] to arbitrary dislocation configurations, to simulate dislocation core structures and various dislocation network configurations at pure twist GBs. Based on the generalized Peierls-Nabarro model, Dai et al. [18] calculated structures of {111}-GBs with different twist angles in Al, Ni and Cu using both the perfect crystal reference and twin reference states, and calculated the corresponding energies of GBs over the full range of twist angles using an interpolation method. Qiu et al. [19] adopted the MPF model in their study of (110) pure twist GBs in five BCC metals, which has allowed them to lift the degeneracy of the geometric models [13,14,20] in predicting GB structures. A general observation from Oiu et al. simulations is that dislocation dissociation is prohibited in BCC metals due to the high SFE and the resulting GND networks at GBs are controlled only by the reaction of full dislocations at the nodal point. However, it is well known that Shockley partial dislocations are commonly observed in FCC metals and complex dislocation reactions are expected in the formation of GND networks at GBs. In the previous work on FCC metals mentioned above [10,18,21], while the GND structure of pure twist {111}-GB in Al exhibits a hexagonal geometry [10], those in Cu and Ni have a triangular morphology [18]. In this paper we investigate a larger group of FCC metals (namely, Ag, Cu, Rh, Ir, Pd, Pt for the parametric study and Au, Ni for the validation) for the dependency of GB dislocation configuration on their GSFE property as well as the misorientation angle. The GB formation mechanisms are analyzed in terms of the underlying dislocation reactions and evolutions. GBs consisting of a whole spectrum from pure screw partial to pure screw full dislocations are revealed, which are found to correlate strongly with the stacking fault energy and the elastic modulus. Fast-acting models are developed to evaluate the configurations of the GND network, as a function of the material properties (i.e., GSFE and elastic constants) and the misorientation angle of GBs.

For FCC metals, SFE is a critical material parameter that is commonly used to describe their plastic deformation behaviors [22]. For example, the easiness of dislocation cross-slip, competition between deformation twinning and dislocation slips and that between dynamic recovery and dynamic recrystallization are all closely related to the value of SFE [23-25]. It is well known that the separation between two Shockley partials in a full dislocation of FCC metals is uniquely determined by the elastic properties and SFE, which is commonly used to estimate the value of SFE based on TEM characterization of the dislocation cores [26]. Therefore, extensive efforts have been made both computationally and experimentally [27-31] in determining SFE in different metals and alloys. However, the extended dislocation configurations observed in the experiments may not be the equilibrium configurations, which may bring errors in the SFE measurements. For dislocation networks at GBs, the GND configurations are in equilibrium and the stacking fault area formed at the GND network may allow one to determine the SFE more accurately in experiments.

The paper is organized as follows. The framework of the phase-field model used in this study is explained in Section 2. In Section 3, we present the model inputs and the main results obtained through our parametric study, followed by some important analyses in Section 4 that account for the physical principals guiding the temporal evolution of GB dislocations and their geometric features at equilibrium. The main findings are summarized in Section 5.

#### 2. Methods

Phase-field (PF) method [32,33] has a great flexibility in describing microstructural nonuniformity due to defects, precipitates and micro zones caused during mechanical processing. The flexibility comes from the fact that in PF models, different heterogeneities are described by phenomenological variables, or, the so-called order parameter *fields*, whose numerical values are distinguished based on physical and chemical properties (e.g., the phase, grain orientation, concentration, etc.) at the local position in the system. In addition, the "diffuse interface" assumption in PF model involves the spread of sharp interfaces in the continuum limit into a smooth interfacial layer, whose motion is governed by variational principles based on energy minimization without the need to explicitly tracking the position of the interfaces. Therefore, PF becomes an ideal way to describe the evolution of complex microstructural nonuniformities at the micro- and *meso*-scale.

In the specific MPF model for a grain boundary, consider that a single crystal is divided into two semi-infinite crystal blocks, which are twisted relative to each other by a small angle ( $\theta=2^\circ$  in the current work) along a certain plane, i.e., the GB plane (GBP). In the current work, we use order parameters  $\eta_{i=1,2}^{\rm rot}$  to describe the displacement field  $\mathbf{u}^{\rm rot}$  caused by rigid-body rotation due to the macroscopic DOF of GBs, and  $\eta_{i=1,2}^{\rm rel}$  to describe the displacement  $\mathbf{u}^{\rm rel}$  due to the microscopic variation of the elastic strain during the relaxation process. Note that  $\eta_{i=1,2}^{\rm rot}$  is a static field variable but  $\eta_{i=1,2}^{\rm rel}$  keeps evolving and is subjected to the periodic boundary condition. At the initial,  $\eta_i^{\rm rot}$  is non-zero but  $\eta_i^{\rm rel}$  is zero. The total displacement field  $\mathbf{u}(\mathbf{r},t)$  is the summation of  $\mathbf{u}^{\rm rot}$  and  $\mathbf{u}^{\rm rel}$ , both of which are the combinations of order parameters and displacement base vectors  $\mathbf{b}_{i=1,2}$ :

$$\mathbf{u}(\mathbf{r},t) = \mathbf{u}^{\text{rot}} + \mathbf{u}^{\text{rel}} = \sum_{i=1,2} \left[ \eta_i^{\text{rot}}(\mathbf{r}) + \eta_i^{\text{rel}}(\mathbf{r},t) \right] \mathbf{b}_i$$
 (1)

The temporal evolution of GB structure is governed by minimizing the total energy of the system consisting of two parts of energies, i.e., the localized inelastic crystalline energy  $E^{\text{cryst}}$  restrained within the GBP, and the long-range elastic strain energy  $E^{\text{el}}$  stored in the bulk:

$$E^{\text{tot}}(\mathbf{r},t) = E^{\text{cryst}} \left[ \mathbf{u}^{\text{rot}}(\mathbf{r}) + \mathbf{u}^{\text{rel}}(\mathbf{r},t) \right] + E^{\text{el}} \left[ \mathbf{u}^{\text{rel}}(\mathbf{r},t) \right]$$
 (2)

The relaxation field  $\mathbf{u}^{\mathrm{rel}}(\mathbf{r},t)$  keeps updating with the order parameters  $\eta_i^{\mathrm{rel}}$  according to Eq. (1) and in return altering the system energy by Eq. (2). The competition between the two energy terms through the evolution of order parameter fields will lead to the equilibrium state of the grain boundary structure. Specifically,  $E^{\mathrm{cryst}}$  is a functional of total displacement at the GBP and determined by the GSFE surface  $\gamma$ :

$$E^{\text{cryst}} = \int \gamma([\mathbf{u}(\mathbf{r}, t)]) dA.$$
 (3)

The GSFE data in the current study is from DFT calculations by Su et al. [34]. For the elastic part, following the Eshelby inclusion approach, the analytical solution for strain energy is a functional of stress-free transformation strain (SFTS)  $\epsilon_{ij}^p$  of dislocations and corresponding order parameters  $\eta_p$  at the reciprocal space, which is expressed as [35]:

$$E^{\text{el}} = \frac{1}{2} \sum_{p,q=1}^{N} \int B_{pq}(\widehat{\mathbf{n}}) \widetilde{\eta}_{p}(\mathbf{g}) \widetilde{\eta}_{q}^{*}(\mathbf{g}) \frac{d\mathbf{g}}{(2\pi)^{3}}$$
(4)

where **g** is the reciprocal vector,  $\hat{\mathbf{n}} \equiv \mathbf{g}/|\mathbf{g}|$ , and  $B_{pq}(\hat{\mathbf{n}}) = C_{ijkl}\epsilon_{ij}^p\epsilon_{kl}^q - n_i\sigma_{ij}^p\Omega_{jk}(\hat{\mathbf{n}})\sigma_{kl}^qn_l$ . The tide  $\sim$  designates the Fourier transform and the asterisk a complex conjugate.  $\sigma_{ij}^p \equiv C_{ijkl}\epsilon_{kl}^T$  with  $C_{ijkl}$  being the elastic stiffness tensor.  $[\Omega_{ik}]^{-1}(\hat{\mathbf{n}}) \equiv C_{ijkl}\hat{n}_j\hat{n}_l$ . The relaxation of the GB structure can be described by the Allen-Cahn equations, which reaches the equilibrium state when the variation of the total energy becomes

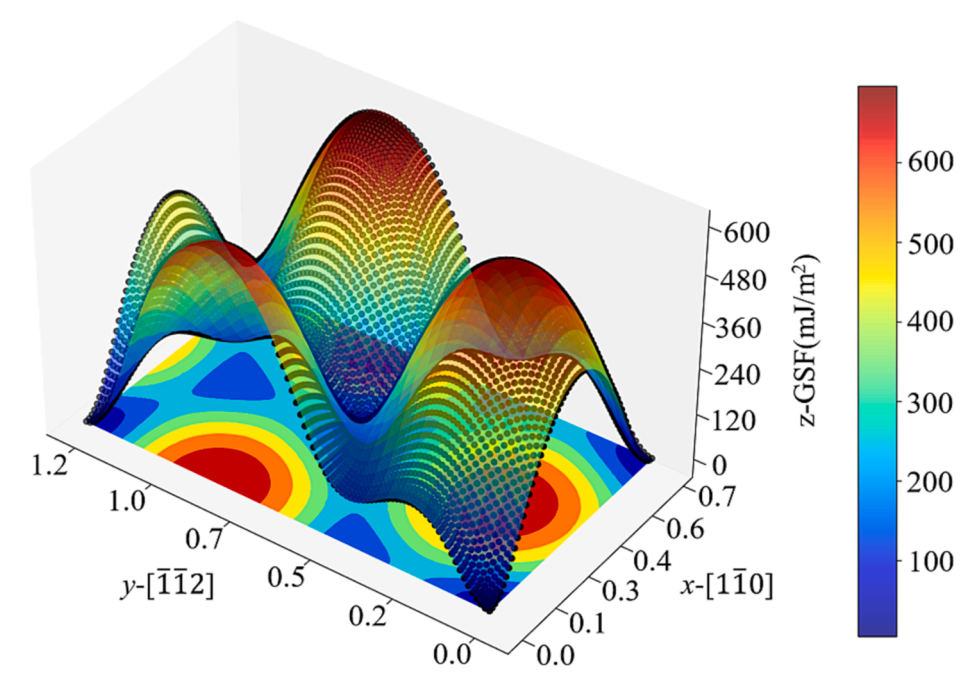


**Fig. 1.** 3D view of the continuous GSFE surface of Pd, fitted according to Eq. (5), using original discrete data (black dots) [34], with  $x \mid |[1\overline{1}0]|$  and  $y \mid |[1\overline{1}2]|$  (units of x and y:  $a_0$ ), z-axis is the GSFE (unit: mJ/m<sup>2</sup>).

Table 1
Fitting parameters of GSFE surface (unit: mJ/m²) of six FCC metals.

Metal	Ag	Cu	Rh	Īr	Pd	Pt
$c_0$	218.931	379.605	693.501	907.23	355.908	376.797
$c_1$	-58.03	-105.4	-140.8	-169.4	-90.43	-88.21
$c_2$	-15.83	-22.7	-88.19	-126.2	-26.1	-31.66
$c_3$	3.255	4.403	7.573	10.36	1.482	1.247
$c_4$	-1.186	-1.419	-4.875	-8.585	-1.794	-3.488
$a_1$	-96.16	-168.5	-177.3	-168.9	-113.2	-66.01
$a_3$	-6.094	-8.868	-23.69	-36.44	-9.197	-18.05

zero, i.e.,  $\frac{\delta E^{\text{tot}}}{\delta \eta_i} = 0$ .

#### 3. Results

#### 3.1. GSFE surface

In this work, the close-packed (111) plane is chosen as the GBP and a periodical repeating rectangular computational cell is defined with the x and y direction parallel to  $[1\overline{1}0]$  and  $[\overline{11}2]$ , respectively, and the ratio of two dimensions, i.e.,  $\frac{l_x}{l_y} = \sqrt{3}$  due to the symmetry of (111) plane, with periodic boundary condition applied to both directions. Due to the variational nature of the PF model, the discrete GSFE datapoints from ab initio calculations need to be equipped with a functional form to characterize a smooth GSFE energy surface. Several methods have been used previously to address this issue [11,19]. In the current study, a Fourier series, originally proposed by Schoeck [36] et al., is used to fit the discrete GSFE data into a continuous function of the displacement in the GBP, which takes the following form:

$$\begin{split} f(x,y) &= \{c_0 + c_1[\cos(2px) + \cos(px + qy) + \cos(px - qy)] \\ &+ c_2[\cos(2qy) + \cos(3px + qy) + \cos(3px - qy)] \\ &+ c_3[\cos(4px) + \cos(2px + 2qy) + \cos(-2px - 2qy)] \\ &+ c_4[\cos(px + 3qy) + \cos(-px + 3qy) + \cos(4px + 2qy) + \cos(-4px + 2qy) \\ &+ \cos(5px + qy) + \cos(5px - qy)] \\ &+ a_1[\sin(2px) - \sin(px + qy) - \sin(px - qy)] \\ &+ a_3[\sin(4px) - \sin(2px + 2qy) - \sin(2px - 2qy)]\}/d, \end{split}$$

 Table 2

 Lattice parameters and elastic constants of six metals.

Metal	Ag	Cu	Rh	Ir	Pd	Pt		
Lattice Parameter (unit: Å)								
$a_0$	4.153	3.634	3.831	3.873	3.942	3.968		
Elastic constants (unit: 10 GPa)								
$c_{11}$	10.05	17.496	40.534	58.365	20.229	29.951		
$c_{12}$	8.525	12.157	18.31	23.436	15.132	22.536		
C44	3.916	7.645	18.747	25.435	6.152	5.985		

Where x and y are the coordinates along  $[1\overline{1}0]$  and  $[\overline{11}2]$ , respectively,  $p=2\pi/(b\sqrt{3})$ ,  $q=2\pi/b$ ,  $b=\frac{a_0}{\sqrt{2}}$  with  $a_0$  being the lattice constant, and d is the interplanar distance of the slip plane (111). Fig. 1 presents a 3D view of the continuous GSFE surface fitted according to Eq. (5), together with original discrete GSFE data (black dots) of metal Pd [34]. The periodically repeated regions with high and low GSF energies exhibit the 3-fold symmetry of {111} planes. The fitting parameters for Pd and other five FCC metals are listed in Table 1. Besides the GSFE surface, the lattice parameters and elastic constants are also required as the input of the current MPF model, which are listed in Table 2.

# 3.2. Evolution of GB dislocation networks

Taking Pd as an example, the very initial microstructure of a twist GB with  $\theta=2^\circ$  at t=1 (reduced time) is shown in Fig. 2(a). During the minimization of the total free energy, the GB morphologies keep

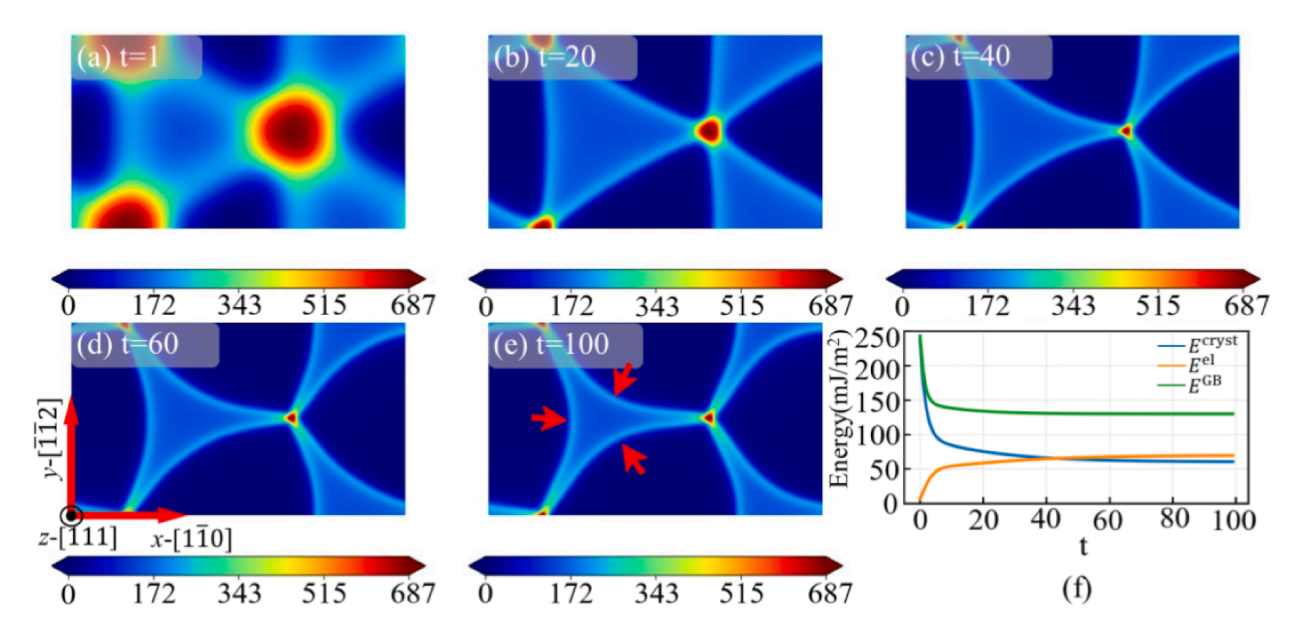


**Fig. 2.** (a-e) The crystalline energy distribution (i.e., the distribution of GB dislocations) at an  $\{111\}$  twist  $(2^{\circ})$  GBP of Pd as a function of evolution time, (f) the corresponding evolution of crystalline energy  $(E^{\text{cryst}})$ , elastic strain energy  $(E^{\text{el}})$  and grain boundary energy  $(E^{\text{GB}})$  (unit: mJ/m<sup>2</sup>).

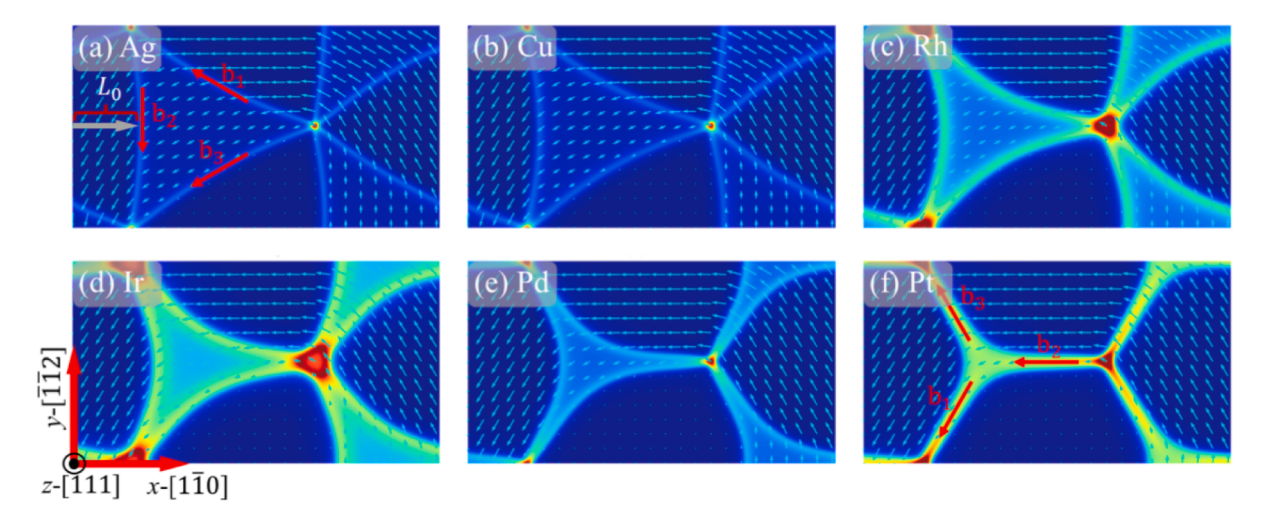


Fig. 3. The configurations of GB dislocations of different FCC metals: (a) Ag, (b) Cu, (c) Rh, (d) Ir, (e) Pd and (f) Pt, the arrows in the figures represent the displacements at corresponding field points.

evolving as presented in Fig. 2(b)-(e) at different time steps, together with the changes in energies during the whole evolution process shown in Fig. 2(f). The values of crystalline energy indicate the degrees of faulting, i.e., zones of zero  $E^{cryst}$  representing the perfect crystal and zones of positive  $E^{cryst}$  representing the cores of dislocations. In Fig. 2, at the initial stage (t = 1), zones with high  $E^{cryst}$  occupy a large percentage of the whole computational cell. It should be noted that the dislocation nodes have the highest  $E^{cryst}$  at fixed positions during the whole process due to the crystal symmetry. During the following evolution, the high E<sup>cryst</sup> zones start to shrink, with the decrease of the total crystalline energy ( $E^{\text{cryst}}$  in Fig. 2(f)) but the increase of the elastic strain energy ( $E^{\text{el}}$  in Fig. 2(f)). After t = 40, the GB dislocations start to curl and the regions between the dislocations, i.e., the stacking fault (SF) regions, become smaller until the equilibrium is reached at t=100. The equilibrium dislocation configuration consists of curved line segments of Shockley partials (as indicated by red arrows in Fig. 2(e)) with a certain width. By examining the GB energy (i.e.,  $E^{\rm GB}$  in Fig. 2(f)), which is the summation of crystalline energy and elastic strain energy, we find that it keeps decreasing all the way from t=1 and converges to around 130  $\mbox{mJ/m}^2$  when the system reaches the equilibrium state.

# 3.3. Characteristics of GB dislocations of different FCC metals

For parametric study, we calculate the equilibrium GB structures of six different metals with inputs listed in Table 1 and Table 2. The corresponding results are shown in Fig. 3. Apparently, even though these metals all have FCC structures, they can form very distinctive GB dislocation network configurations. To further analyze the characteristics of GB dislocation networks for different metals, we superimpose the displacement fields at equilibrium for all these metal systems in Fig. 3, which are denoted by the white arrows. Note that the length and direction of the displacement vectors represent the magnitude and direction of displacement at each position, respectively. Unlike the geometric methods (e.g., O-lattice theory or Frank-Bilby equations), where the

**Table 3** GB energies of six FCC metals with  $\theta=2^{\circ}$ .

Material	Ag	Cu	Rh	Ir	Pd	Pt
$E^{GB}$ (unit: mJ/m <sup>2</sup> ))	56.2	111.5	346.2	510.7	130.0	160.8

Burgers vectors are set as the inputs of the model, our MPF model can output the displacements, thus the Burgers vectors, at each step of evolution. Upon equilibrium, the order parameter  $\eta^{\rm rel}$  stops evolving. We then output the equilibrium  $\eta^{\rm rel}$  and the static background order parameter  $\eta^{\rm rot}$  to calculate the displacement field according to Eq. (1). As can be seen in Fig. 3, the displacements in the whole (111) plane at equilibrium are regionalized: the boundaries of adjacent regions are separated by dislocations with different configurations and within each region, the displacements at each field point are identical. The Burgers vectors associated with the dislocations at the region boundaries can be identified simply by calculating the displacement differences between adjacent region centers.

Unlike the cases in BCC metals, where the Burgers vectors associated with those GB dislocations are identical for all metals belonging to the same crystal structure [19], the GB dislocations in FCC metals can be either Shockley partials or full dislocations. For example, as shown by the red arrows in Fig. 3(f), the GB dislocations in Pt are full dislocations, with the Burgers vectors determined to be  $\mathbf{b}_1 = \frac{[011]}{2}a_0$ ,  $\mathbf{b}_2 = \frac{[110]}{2}a_0$  and  $\mathbf{b}_3 = \frac{[\overline{1}01]}{2}a_0$ ; for Ag, as in Fig. 3(a), however, the GB dislocations are partial dislocations, with the Burgers vectors being  $\mathbf{b}_1 = \frac{[\overline{2}11]}{6}a_0$ ,  $\mathbf{b}_2 = \frac{[11\overline{2}]}{6}a_0$  and  $\mathbf{b}_3 = \frac{[\overline{1}2\overline{1}]}{6}a_0$ . Therefore, stacking faults can be seen among partial dislocations in Ag-(111) but missing in the case of Pt. Dislocations with the above configurations are commonly observed in FCC crystals. It is obvious that although the dislocations in Ag are partial

ones but those in Pt are full ones, all the dislocations in these two cases have the feature of almost pure screw dislocations. In contrast, the curved dislocations in other cases (especially those in Rh, Ir and Pd) are of the mixed type. The calculated structure of the twist GB in Cu agrees well with the previous work done by Dai et al. [18], where the GB dislocation in Cu also show a triangular network. We will further analyze the geometric features concerning the GB dislocation networks and their relationships with the material properties (i.e., the GSFE surface and the elastic constants) and GB misorientation angle  $\theta$  in the Discussion Section. Apart from the dislocation sense directions and the corresponding Burgers vectors, the GB energies  $E^{GB}$  of these metals are shown in Table 3. As can be seen in Table 3, the magnitude of the GB energy varies greatly for different metal systems, since the crystalline energy and elastic strain energy are closely related to the stacking fault energy and elastic constants of materials, both of which vary greatly from metal to metal.

#### 4. Discussion

# 4.1. Quantification of the size of stacking fault regions

To find a direct relationship between the GSFE surface and the dislocation network configuration, we first plot the GSFE curves of the six metals in the direction of  $[\overline{11}2]$  in Fig. 4(a). The stacking fault energy  $(\gamma_{\rm sf})$  is specified in the curve (taking Ir as an example) by the red arrow, together with the cooresponding values shown in Fig. 4(b). Note that we denote the ratio of  $\gamma_{\rm sf}$  and  $\mu b$  as the reduced stacking fault energy  $\overline{\gamma}_{\rm sf}$ , where b is the magnitude of the Burgers vector  $(b=\frac{\sqrt{2}}{2}a_0)$  and  $\mu=1/5(c11+3c44-c12)$  for cubic crystals [37].

Comparing Fig. 4(b) with Fig. 3, we can find that the dislocation dissociation is harder to take place in metals with larger  $\bar{\gamma}_{sf}$ , resulting in

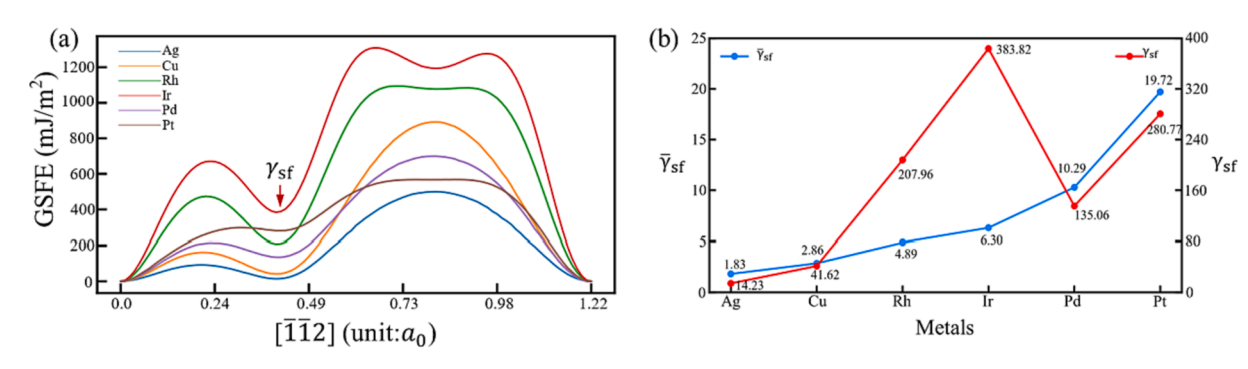
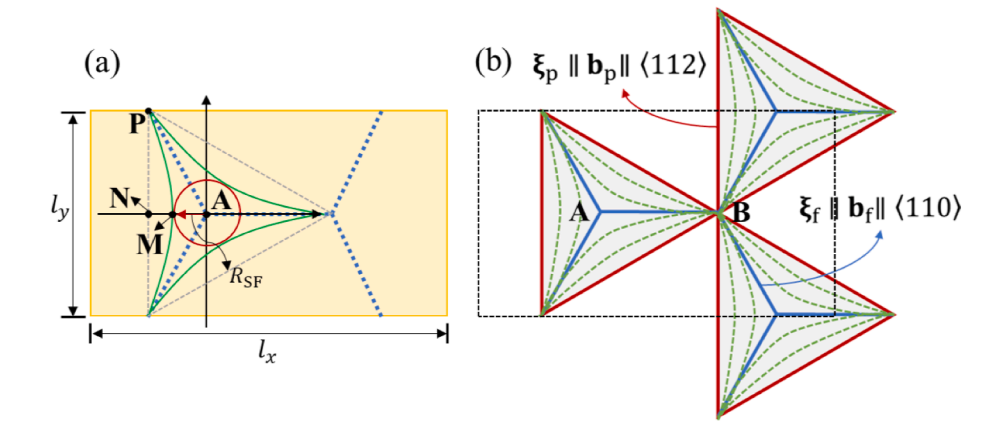
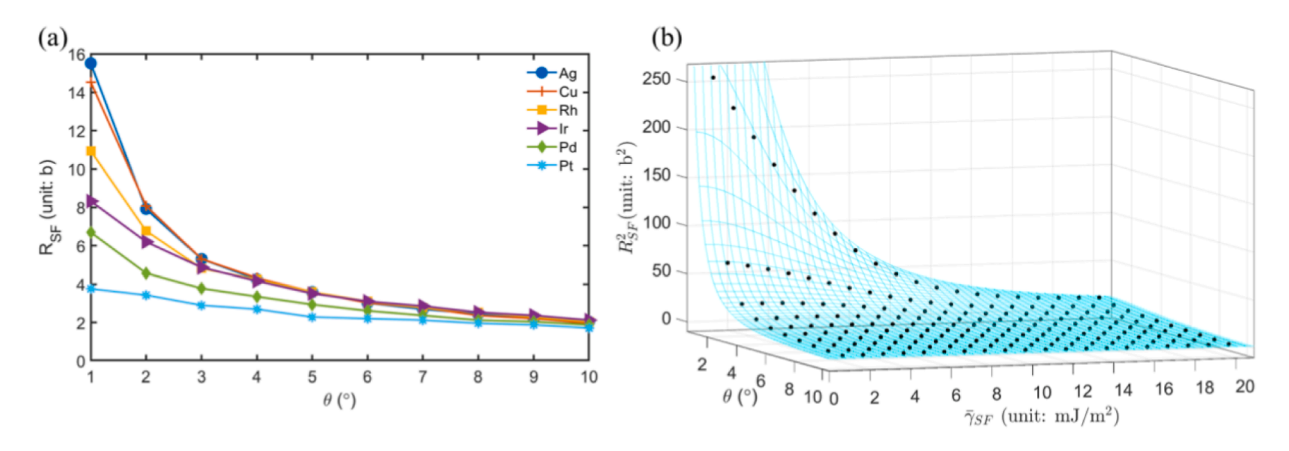


Fig. 4. (a) GSFE curves of six metals in the direction of  $[\overline{11}2]$ , (b) the values of stacking fault energy  $(\gamma_{sf})$  and the reduced stacking fault energy  $(\overline{\gamma}_{sf} = \frac{\gamma_{sf}}{\mu b})$  of the six metals.



**Fig. 5.** (a) Schematic drawing of the GB dislocation lines (green) and the incircle (red) of a stacking fault region surrounded by the partial dislocations with the computational cell parameters of  $l_x$  and  $l_y$ , (b) possible configurations of GB dislocation networks in FCC metals, including two extreme cases (solid red and blue lines) and general cases (dashed green curves). (The coordinate in (a) with the origin set at A is for latter discussion.). (For interpretation of the references to colour in this figure legend, the reader is referred to the web version of this article.)



**Fig. 6.** (a) the relationship between incircle radius  $R_{\rm sf}$  and misorientation  $\theta$  for different metals, (b) the fitted  $R_{\rm sf}^2$  surface as a function of  $\bar{\gamma}_{\rm sf}$  and  $\theta$  according to Eq. (6) with fitting parameter m=14.84.

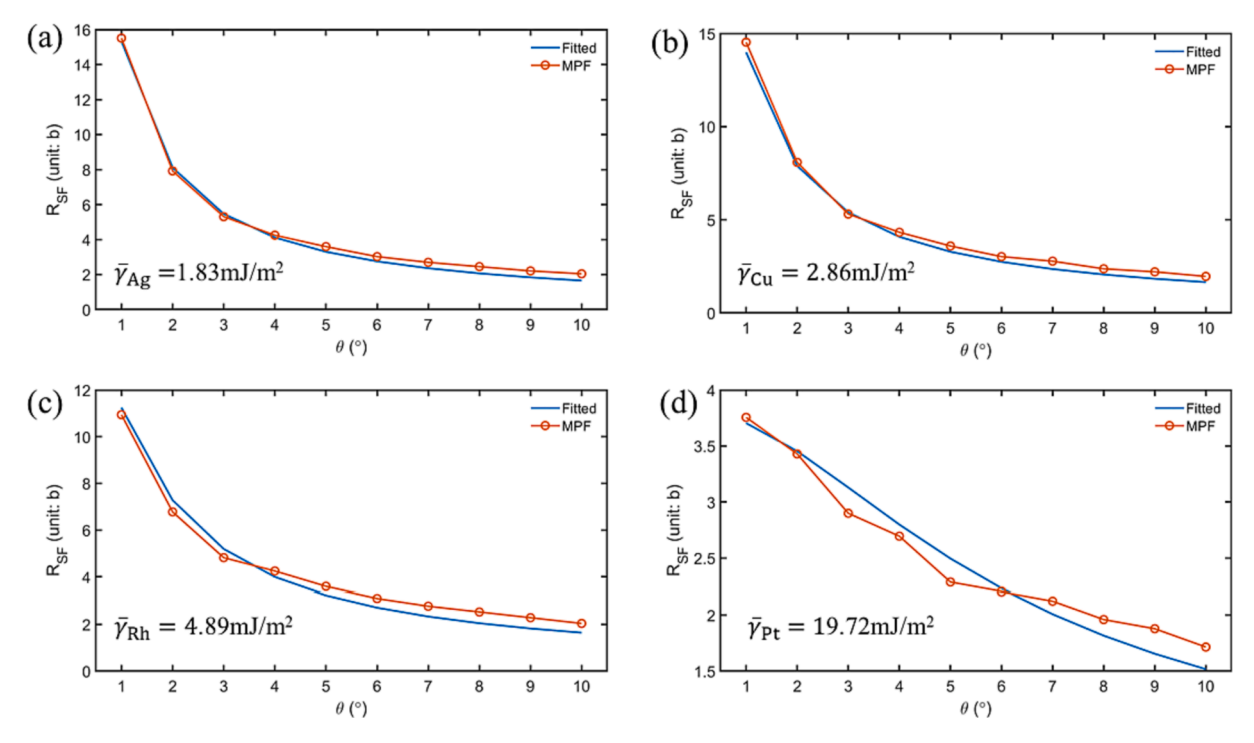


**Fig. 7.** The comparison between the fitted  $R_{sf}$  according to Eq. (6) and the measured value directly from the current MPF model for different metals: (a) Ag, (b) Cu, (c) Rh and (d) Pt.

smaller stacking fault regions. To quantify the size of stacking fault region, we draw an incircle with radius of  $R_{\rm sf}$  within the faulted region, as schematically shown in Fig. 5(a), based on the distribution of the crystalline energy shown in Fig. 3. With different values of  $R_{\rm sf}$ , the GNDs within the twist GB can form hexagonal (solid blue lines) or triangular (solid red lines) networks, or configurations in between (dashed green lines), as shown in Fig. 5(b). On the other hand, precious work by Dai et al. [38] has shown that the misorientation angle  $\theta$  also plays an important role in the structure of GB dislocation networks. Therefore, a parametric study with  $\theta=1~10^\circ$  has been carried out for all the above metals. The calculation result shows that for a given metal system,  $R_{\rm sf}$  exhibits a negative correlation with the increase in both  $\theta$  and  $\overline{\gamma}_{\rm sf}$ , as shown in Fig. 6 (a). To incorporate both the effects of material property  $\overline{\gamma}_{\rm sf}$  and misorientation  $\theta$ , two special cases should be firstly considered:

- Case-I: ¬¬sf→∞, R<sub>sf</sub>→0, indicating no dislocation dissociation takes place due to high ¬¬sf and a hexagonal network will form, with the junction of dislocations located at "A" in Fig. 5(a).
- Case-II:  $\overline{\gamma}_{sf} \rightarrow 0$ ,  $R_{sf} \rightarrow \frac{1}{6}l_x$  (with  $l_x = \frac{\sqrt{3}b}{\theta}$  being the periodic length of the computational cell in the direction of  $[1\overline{1}0]$ ), indicating dislocation dissociation takes place thoroughly and a triangular network will form with the point of tangency being "N" in Fig. 5(a).

These two special cases correspond to the dislocation networks shown in Fig. 5(b) with blue and red solid lines, respectively. Based on the above analysis, we assume the magnitude of  $R_{\rm sf}^2$  as a function of  $\overline{\gamma}_{\rm sf}$  (J/m²) and  $\theta$  (rad) is in the form of:

$$R_{\rm sf}^2 = \frac{b^2}{12\left(m\overline{\gamma}_{\rm sf}^2 + \theta^2\right)} \tag{6}$$

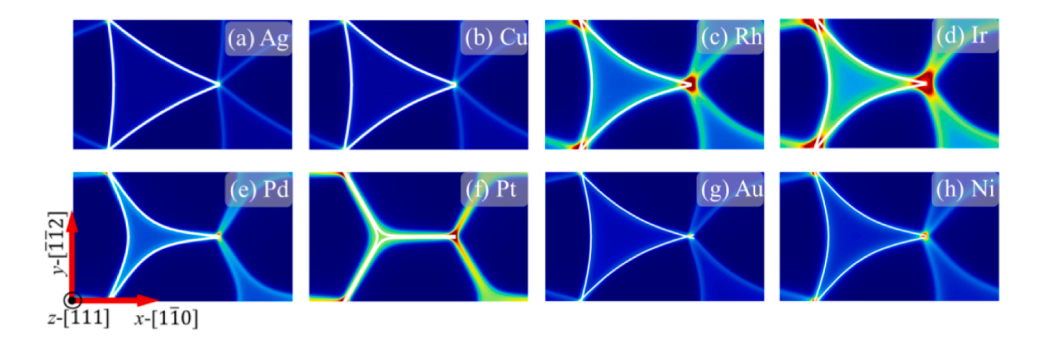


Fig. 8. The prediction of geometric GB dislocation lines based on the reduced stacking fault energy  $\overline{\gamma}_{sf}$  with  $\theta=2^{\circ}$  for (a) Ag, (b) Cu, (c) Rh, (d) Ir, (e) Pd, (f) Pt, (g) Au and (h) Ni.

With the fitting parameter m=14.84, the fitted surface  $R_{\rm sf}^2$  as a function of  $\overline{\gamma}_{\rm sf}$  and  $\theta$  based on Eq. (6) is shown in Fig. 6(b) with the black dots suggesting the values of  $R_{\rm sf}^2$  with  $\theta$  ranging from 1° to 10° and  $\overline{\gamma}_{\rm sf}$  from 1.0 to 20.0 mJ/m². The coefficient of determination R-Squared of Eq. (6) is  $\sim 0.99$ , indicating that Eq. (6) is a good approximation to  $R_{\rm sf}^2$ . Fig. 7 compares the fitted  $R_{\rm sf}$  as a function of  $\theta$  for Ag, Cu, Rh and Pt metals according to Eq. (6) with the measured  $R_{\rm sf}$  from our MPF model. For metals with smaller  $\overline{\gamma}_{\rm sf}$ , the fitted  $R_{\rm sf}$  agrees well with our simulation data (see Fig. 7(a)-(c)). However, for metal with a larger  $\overline{\gamma}_{\rm sf}$  (e.g., Pt) the deviation of fitted  $R_{\rm sf}$  from the simulation result is relatively larger, mainly due to the resolution issue of the model in measuring the value of  $R_{\rm sf}$  when  $R_{\rm sf}$  is as small as 1b  $\sim$  4b (Fig. 7(d)).

To quantitatively characterize the degree of dislocation dissociation taking place in different metals within the twist GBs under different misorientation angles, and with the above two special cases being considered, we introduce a parameter defined by the ratio of  $R_{\rm sf}^2$  over its limit value of  $(R_{\rm sf}^2)_{\rm max} = \frac{b^2}{12\rho^2}$  (corresponding to special Case-II):

$$\rho = \frac{R_{\rm sf}^2}{(R_{\rm sf}^2)_{\rm min}} = \left(m\bar{\gamma}_{\rm sf}^2 + \theta^2\right)^{-1} \tag{7}$$

The degree of dislocation dissociation  $\rho$  decays with both increasing  $\overline{\gamma}_{\rm sf}$  and  $\theta$ . In other words, for a given misorientation angle  $\theta$ ,  $\rho$  is approaching zero when  $\overline{\gamma}_{\rm sf}$  is infinitely large and dislocations do not dissociate at all; on the contrary,  $\rho$  reaches the maximum value of  $\frac{1}{\theta^2}$  when  $\overline{\gamma}_{\rm sf}$  is zero and dislocation dissociation takes place completely. Importantly, with known misorientation angle  $\theta$ , Eq. (6) also provides a possible way to calculate the value of  $\gamma_{\rm sf}$  for FCC materials if we can measure the size of stacking fault region at twist GBs from experiments and evaluate the value of  $R_{\rm sf}$ .

# 4.2. A fast-acting model for the predictions of GB dislocation network configurations

Due to the computational complexity of the above full MPF modeling, it is desirable to obtain an approximate model to predict the equilibrium configurations of GB dislocation networks and GB energy directly and simply via the GSFE data, GB misorientation angle and elastic constants. The geometric features concerning the curvature of dislocation lines within the network (see Fig. 3 obtained by our MPF model and Fig. 5(b) for schematic drawings and analysis) shows the characteristics of bow-shaped curves described by the equation of hyperbola. Therefore, by neglecting the diffuse core structure and treat dislocations as geometric lines dividing perfect crystal and faulted regions, we introduce a hyperbola function to describe the shape of those dislocation lines, since the concave-convex degree of the partial dislocation lines can be directly correlated with the  $\bar{\gamma}_{sf}$  of materials and the misorientation angle  $\theta$ . As shown in Fig. 5(a), by setting the origin at Point A the incircle radius  $R_{sf}$  equals the length of transverse axis. With

the standard form of a hyperbola function, we can then derive the length of conjugate axis  $\lambda$  by substituting the coordinate of P ( $-\frac{1}{6}l_x,\frac{1}{2}l_y$ ), which is a fixed point due to the symmetry of the {1 1 1} planes in FCC crystals:

$$\frac{x^2}{R_{\rm sf}^2} - \frac{y^2}{\lambda^2} = 1, \text{ with } \begin{cases} R_{\rm sf}^2 = \frac{b^2}{12\left(m\overline{\gamma}_{\rm sf}^2 + \theta^2\right)} \\ \lambda^2 = \frac{b^2}{4m\overline{\gamma}_{\rm sf}^2} \end{cases}$$
(8)

As can be seen in Eq. (8), while the variation in the length of transverse axis  $R_{\rm sf}$  depends on both  $\overline{\gamma}_{\rm sf}$  and  $\theta$ , the length of the conjugate axis  $\lambda$  is independent of  $\theta$ . Based on Eq. (8), the asymptote equation can be derived by the ratio of  $\lambda$  over  $R_{\rm sf}$ , i.e.,  $y=\pm\sqrt{3+\frac{3}{m}}\bullet\frac{\theta^2}{\overline{\gamma}_{\rm sf}^2}x$ . The slope of the asymptote, i.e.,  $\sqrt{3+\frac{3}{m}}\bullet\frac{\theta^2}{\overline{\gamma}_{\rm sf}^2}$ , decreases monotonically from  $\infty$  when  $\overline{\gamma}_{\rm sf}\to 0$  and reaches to  $\sqrt{3}$  when  $\overline{\gamma}_{\rm sf}\to \infty$ , which corresponds to the evolution in dislocation network configurations in Fig. 5(b) from triangular (solid red) to curved triangular (dashed green) and finally to hexagonal (solid blue) network. From the above analysis, one can expect that Eq. (6) gives a quantitative description of the size of stacking fault region and the point of tangency M in Fig. 5(a) and, on the other hand, Eq. (8) describes the shapes of the dislocation networks with known material property  $\overline{\gamma}_{\rm sf}$  and GB misorientation  $\theta$ .

Using the above fast-acting method by Eq. (6) and (8), we predict twist GB dislocation networks (white solid lines in Fig. 8) for eight metals (with additional two metals of Ni and Au) with  $\theta=2^\circ$  and the results are shown in Fig. 8 in comparison with the predictions from the MPF simulations. The agreement is excellent. Such a method provides one a quick way to link material properties to the structure of GBs, which is an important input required by some physics-based models such as crystal plasticity model and GB segregation model.

# 5. Conclusions

By incorporating the generalized stacking fault energy (GSFE) surfaces from DFT calculations in the microscopic phase field (MPF) model, we are able to predict detailed configurations of GND networks of low-angle twist GBs and their energies for different FCC metals. The main findings include:

(1) The GB dislocations network configurations in FCC metals varies from triangular networks consisting of pure screw Shockley partial dislocations to hexagonal networks consisting of pure screw full dislocations, with various of intermediate configurations consisting mixed Shockley partial dislocations, depending on their GSFE surfaces. For example, a triangular dislocation network forms in Ag with partial dislocations ( $\mathbf{b} = \frac{1}{6} \langle \overline{112} \rangle$ ) surrounding stacking fault regions, and a hexagonal network form in

- Pt with full dislocations ( $\mathbf{b} = \frac{1}{2} \langle \overline{1}10 \rangle$ ). The partial and full dislocations in Ag and Pt are both pure screw type.
- (2) The transition from triangular to hexagonal dislocation networks is analyzed, which suggests that the value of the reduced stacking fault energy (defined as the ratio of stable stacking fault energy over μb) determines the configuration of the GB dislocation networks and thus the areas of the corresponding stacking fault regions. More specifically, a larger reduced stacking fault energy would prefer a hexagonal network consisting of full dislocations, while a smaller one would prefer a triangular network consisting of Shockley partial dislocations.

Based on the simulation results, a fast-acting analytical model is formulated for predicting GB dislocation network configurations as a function of the elastic constants, stacking fault energy and misorientation angle. The model is validated for two additional FCC metals against MPF model predictions. The analytical model could be useful for a quick and accurate access to detailed configurations of GB dislocation networks of FCC metals and alloys.

#### CRediT authorship contribution statement

Yongxiang Li: Investigation, Writing – original draft. Di Qiu: Conceptualization, Writing – review & editing, Supervision. Yunzhi Wang: Supervision.

## **Declaration of Competing Interest**

The authors declare that they have no known competing financial interests or personal relationships that could have appeared to influence the work reported in this paper.

#### Data availability

The data that has been used is confidential.

# Acknowledgement

YL and DQ would like to thank the financial supports by the National Key Research and Development Program of China under Grant No. 2022YFB3707803, the Key Research Project of Zhejiang Laboratory under Grant No. 2021PE0AC02, and the National Natural Science Foundation of China under Grant No. U2230102. YW acknowledges the support by the US National Science Foundation (Grant DMR-1923929), which has facilitated this international collaboration.

# Data availability statement

The raw/processed data required to reproduce these findings cannot be shared at this time as the data also forms part of an ongoing study.

# References

- T. Watanabe, Grain boundary engineering: historical perspective and future prospects, J. Mater. Sci. 46 (12) (2011) 4095–4115.
- [2] V.V. Bulatov, B.W. Reed, M. Kumar, Grain boundary energy function for fcc metals, Acta Mater. 65 (2014) 161–175.
- [3] A.J. Vattré, M.J. Demkowicz, Determining the Burgers vectors and elastic strain energies of interface dislocation arrays using anisotropic elasticity theory, Acta Mater. 61 (14) (2013) 5172–5187.
- [4] F. Cao, Y. Chen, S. Zhao, E. Ma, L. Dai, Grain boundary phase transformation in a CrCoNi complex concentrated alloy, Acta Mater. 209 (2021).

- [5] M. Shiga, M. Yamaguchi, H. Kaburaki, Structure and energetics of clean and hydrogenated Ni surfaces and symmetrical tilt grain boundaries using the embedded-atom method, Phys. Rev. B 68 (24) (2003).
- [6] M.A. Tschopp, D.L. McDowell, Asymmetric tilt grain boundary structure and energy in copper and aluminium, Phil. Mag. 87 (25) (2007) 3871–3892.
- [7] D. Wolf, S. Phillpot, Role of the densest lattice planes in the stability of crystalline interfaces: A computer simulation study, Mater. Sci. Eng. A 107 (1989) 3–14.
- [8] E.A. Holm, G.S. Rohrer, S.M. Foiles, A.D. Rollett, H.M. Miller, D.L. Olmsted, Validating computed grain boundary energies in fcc metals using the grain boundary character distribution, Acta Mater. 59 (13) (2011) 5250–5256.
- [9] D.L. Olmsted, S.M. Foiles, E.A. Holm, Survey of computed grain boundary properties in face-centered cubic metals: I. Grain boundary energy, Acta Materialia 57 (13) (2009) 3694–3703.
- [10] C. Shen, J. Li, Y. Wang, Predicting structure and energy of dislocations and grain boundaries, Acta Mater. 74 (2014) 125–131.
- [11] C. Shen, Y. Wang, Incorporation of γ-surface to phase field model of dislocations: simulating dislocation dissociation in fcc crystals, Acta Mater. 52 (3) (2004) 683–691
- [12] W. Bollmann, Crystal defects and crystalline interfaces, Springer Science & Business Media, 2012.
- [13] B.A. Bilby, R. Bullough, E. Smith, Continuous distributions of dislocations: a new application of the methods of non-riemannian geometry, Proc. Roy. Soc. A: Math. Phys. Eng. Sci. 231 (1185) (1955) 263–273.
- [14] F.C. Frank, Martensite, Acta Metall. 1 (1) (1953) 15-21.
- [15] M.F. Ashby, F. Spaepen, S. Williams, The structure of grain boundaries described as a packing of polyhedra, Acta Metall. 26 (11) (1978) 1647–1663.
- [16] A.D. Banadaki, S. Patala, A three-dimensional polyhedral unit model for grain boundary structure in fcc metals, npj Comput. Mater. 3 (1) (2017).
- [17] R. Peierls, The size of a dislocation, Proceedings of the Phys. Soc. 52(1) (1940) 34 %@ 0959-5309.
- [18] S. Dai, Y. Xiang, D.J. Srolovitz, Atomistic, generalized Peierls-Nabarro and analytical models for (111) twist boundaries in Al, Cu and Ni for all twist angles, Acta Mater. 69 (2014) 162–174.
- [19] D. Qiu, P. Zhao, C. Shen, W. Lu, D. Zhang, M. Mrovec, Y. Wang, Predicting grain boundary structure and energy in BCC metals by integrated atomistic and phasefield modeling, Acta Mater. 164 (2019) 799–809.
- [20] W.X. Bollmann, Crystal lattices, interfaces, matrices, Bollmann (1982).
- [21] C. Shen, Y. Wang, Phase field model of dislocation networks, Acta Mater. 51 (9) (2003) 2595–2610.
- [22] S. Suwas, A. Bisht, G. Jagadeesh, Microstructural changes in materials under shock and high strain rate processes: recent updates, Mech. Mater. Modern Manuf. Methods Process. Techniques (2020) 361–392.
- [23] F.J. Humphreys, M.X. Hatherly, Recrystallization and related annealing phenomena. Elsevier. 2012.
- [24] R. Madhavan, R.K. Ray, S. Suwas, New insights into the development of microstructure and deformation texture in nickel–60 wt.% cobalt alloy, Acta Mater. 78 (2014) 222–235.
- [25] R. Madhavan, S. Suwas, Deformation of nanograined Ni-60Co alloy with low stacking fault energy, Philos. Mag. Lett. 94 (2014) 548-555.
- stacking fault energy, Philos. Mag. Lett. 94 (2014) 548–555.

  [26] M. Shih, J. Miao, M. Mills, M. Ghazisaeidi, Stacking fault energy in concentrated alloys, Nat Commun 12 (1) (2021) 3590.
- [27] H. Van Swygenhoven, P.M. Derlet, A.G. Frøseth, Stacking fault energies and slip in nanocrystalline metals, Nat. Mater. 3 (6) (2004) 399–403.
- [28] P. Heino, L.F. Perondi, K.K. Kaski, E. Ristolainen, Stacking-fault energy of copper from molecular-dynamics simulations, Phys. Rev. B 60 (1999) 14625–14631.
- [29] P.J. Ferreira, P. Müllner, A thermodynamic model for the stacking-fault energy, Acta Mater. 46 (13) (1998) 4479–4484.
- [30] J. Lu, L. Hultman, E. Holmström, K.H. Antonsson, M. Grehk, W. Li, L. Vitos, A. Golpayegani, Stacking fault energies in austenitic stainless steels, Acta Mater. 111 (2016) 39–46.
- [31] S.F. Liu, Y. Wu, H.T. Wang, J.Y. He, J.B. Liu, C.X. Chen, X.J. Liu, H. Wang, Z.P. Lu, Stacking fault energy of face-centered-cubic high entropy alloys, Intermetallics 93 (2018) 269–273.
- [32] L.-Q. Chen, Phase-field models for microstructure evolution, Annu. Rev. Mat. Res. 32 (1) (2002) 113–140.
- [33] Y. Wang, J. Li, Phase field modeling of defects and deformation, Acta Mater. 58 (4) (2010) 1212–1235.
- [34] Y. Su, S. Xu, I.J. Beyerlein, Density functional theory calculations of generalized stacking fault energy surfaces for eight face-centered cubic transition metals, J. Appl. Phys. 126 (10) (2019).
- [35] A.G. Khachaturyan, Theory of Structural Transformations in Solids (1983).
- 36] G. Schoeck, The core structure, recombination energy and Peierls energy for dislocations in Al, Philos. Mag. A 81 (5) (2001) 1161–1176.
- [37] J.P. Hirth, Theory of dislocations, J. Appl. Mech. 50 (1983) 476.
- [38] S. Dai, Y. Xiang, D.J. Srolovitz, Structure and energy of (1 1 1) low-angle twist boundaries in Al Cu and Ni, Acta materialia 61 (4) (2013) 1327–1337.